

See discussions, stats, and author profiles for this publication at: <https://www.researchgate.net/publication/261722178>

Evaporation-Induced Branched Structures from Sessile Nanofluid Droplets

ARTICLE *in* THE JOURNAL OF PHYSICAL CHEMISTRY C · MARCH 2013

Impact Factor: 4.77 · DOI: 10.1021/jp312021w

CITATIONS

10

READS

50

2 AUTHORS:



Alexandru Crivoi

Nanyang Technological University

19 PUBLICATIONS 165 CITATIONS

[SEE PROFILE](#)



Fei Duan

Nanyang Technological University

24 PUBLICATIONS 315 CITATIONS

[SEE PROFILE](#)

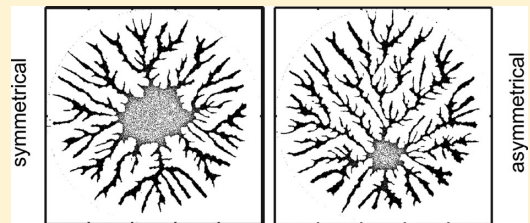
Evaporation-Induced Branched Structures from Sessile Nanofluid Droplets

A. Crivoi and Fei Duan*

School of Mechanical and Aerospace Engineering, Nanyang Technological University, Singapore 639798

 Supporting Information

ABSTRACT: We investigate the formation of branched nanoparticle aggregates resulting from the evaporation of sessile nanofluid droplets of the copper water-based nanofluids experimentally. Both symmetric and asymmetric drying patterns were found as the sessile droplet evaporated. A kinetic Monte Carlo (KMC) approach is developed to explain the drying process in a circular domain, representing the top view of a drying sessile droplet. It is found that the lattice-gas-based Monte Carlo model can describe the nanoparticle self-assembly into a solid highly branched aggregate. While the chemical potential function is coupled to the nondimensional spherical droplet size during evaporation, the results reveal that the fingering contact line instabilities can emerge under a given condition and force the formation of a branched nanoparticle structure. The pattern comparison shows that the simulation results have a qualitative agreement with the experiments. The parameter study shows that the model parameters, such as domain diameter, chemical potential distribution, particle interaction energy, and so on, have significant influence on the resulting patterns.



INTRODUCTION

During nanofluid evaporation, the dispersed nanoparticles can self-assemble into various complex structures.^{1–5} Among them, the coffee-ring pattern^{6,7} was observed after full drying of the pinned colloidal droplets,^{8,9} while the other structures, such as networks, worm-like and ribbon-like islands, or fractal cavities and aggregates, were reported in the experiments with the nanofluid drying.^{10–13} More sophisticated multicomponent structures appeared in dried blood spots¹⁴ and protein samples.¹⁵ The behavior of the moving drying front and deposition of the dispersed nanoparticles was investigated in the previous simulation and experimental works as well.^{10,13,16–20} The applied models include KMC,^{10,13,16,19} dynamical-density functional theory (DDFT),²⁰ and hydrodynamic thin film model.^{17,21,22} Theoretically, the previous KMC works used different settings, such as homogeneous and heterogeneous evaporation,²³ “pseudo-3D” model,¹⁹ fully-3D model,²⁴ and so on, to explore the drying of thin films, including the dewetting process of straight liquid front with a constant chemical potential,¹⁶ the formation of fractal cavities,¹⁹ and the formation of dual-scaled patterns.¹⁰ The other modifications applied a nonconstant chemical potential depending on the global liquid coverage, featuring the sigmoid jump.¹⁰ Presently, to simulate the drying pattern of a sessile droplet with a maximum height at the center of symmetry and a shrinking three-phase line, we introduce a KMC model modification that involves linear chemical potential changes in time and space and investigates evaporation of a macroscopic droplet with a non-negligible thickness profile. The spherical shape of a sessile droplet is taken into account, and the various pattern formation is obtained in simulations with the different

parameter settings, including the varied chemical potential function, the domain diameter, and so on. Simultaneously, the branched structures are investigated experimentally. The experimental and simulation results are compared both qualitatively and using the quantitative analysis of the mass-radius dependency.

EXPERIMENTAL METHODS

In the experiments, the suspensions of 25 nm copper nanoparticles (Nanostructured and Amorphous Materials, Inc.) in the deionized water were prepared into the 0.1% nanofluid in mass concentration. The nanoparticle sample preparation is carried out by using a sensitive mass balance with an accuracy of 0.1 mg. The detailed process was described.^{25,26} Simply speaking, the mixed nanofluids with the mass concentration at 0.1% were well stirred first and then kept in an ultrasonication bath (Fisher Scientific model 500) for more than 2 h to ensure the even initial dispersion of the nanoparticles in the base fluid. The silicon wafer was used as a substrate for the nanofluid sessile droplet drying. To prevent the following agglomeration with time, right after the suspensions were prepared, we placed a tiny sessile droplet with 1 mm or less in diameter and ~30° in contact angle on a clean substrate to dry naturally, as shown in the inset of Figure 1. The drying is performed in the open conditions at 25 °C in temperature, 1 atm in pressure, and 40% in relative humidity.

Received: December 6, 2012

Revised: March 17, 2013

Published: March 21, 2013



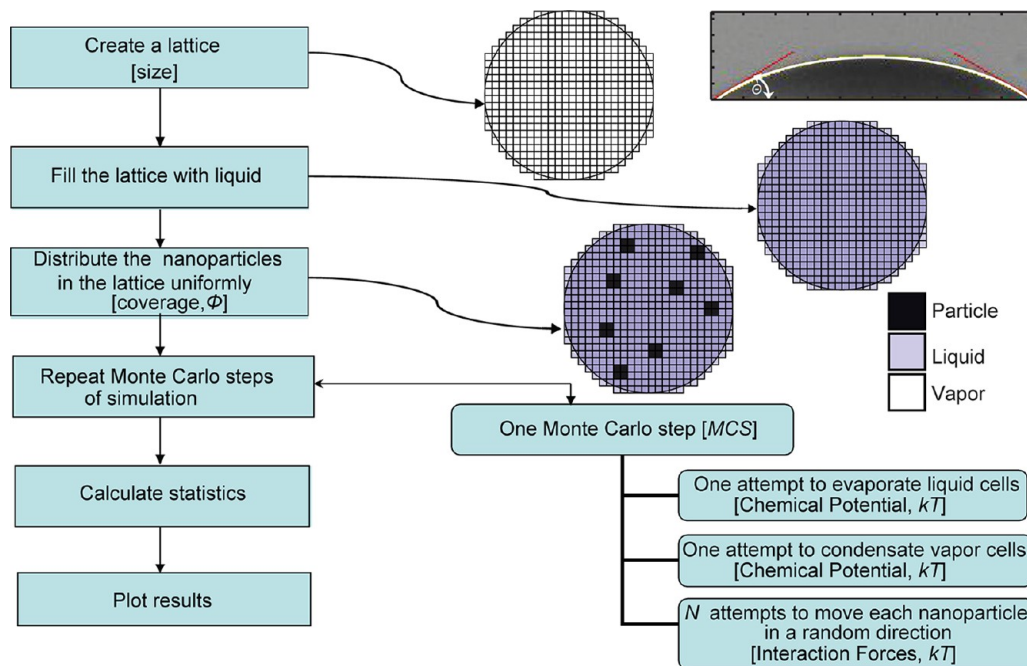


Figure 1. Schematics of the KMC simulation process in a circular domain. The side view of a sessile nanofluid droplet on the substrate is shown in the inset.

The drying patterns were directly recorded with the optical microscope (Zeiss Axioscop II).

MODEL

A mathematical model is developed from the 2D lattice-gas KMC model, introduced by Rabani et al.²³ The flowchart in Figure 1 displays the main procedures of the simulation program. First, an empty domain is created based on the size of lattice, a parameter to be studied. Then, it is filled with the liquid phase. In the next step, some spaces are randomly filled with the particles. The total number of particles depends on the global particle coverage, ϕ , to be defined in the simulation. After that, the loop of repeating Monte Carlo steps starts. The total Monte Carlo step (MCS) number is predefined initially. On each step of the loop, one attempt to change the state of the solvent is performed for each cell of the lattice; then, each particle is moved in a random direction or left in rest depending on the values of the calculated random expressions. The Monte Carlo loop can be stopped for a comparison with the experimental pattern; then, the final statistics are calculated based on the image analysis.

We have to notice a significant difference in the total number of particles with the simulated and experimental structures. The nanoparticle has the real size in the experiments, but the particle in the simulation is dimensionless. This Monte Carlo simulation is to show the main tendencies of the branched structures formation and to investigate the influence of various parameters. The parameter study shows that the branched morphology is present in the simulation domains of different size because the computational resources do not allow us to perform the direct simulation inside the domain with the dimensions correspondent to the size of 850 μm for an example, equivalent to a lattice of the size around 60 000 \times 60 000 cells. The simulations in smaller domains are proposed to resemble the actual experimental process qualitatively. The measurements show that the average width of the actual

experimental finger is in range of 5–20 μm and therefore is comparable with a chain from 200 to 800 original particles. The width of simulated fingers is at least one order of magnitude smaller. Because the trend of the parameter study shows that branched structures might be formed in a lattice domain of any larger size, the qualitative comparison is possible. For a quantitative comparison, the metric characterizing for the compactness of the structure is calculated. It indicates how fast the mass of the branched structure grows in respect to the distance from the center.

In the model, each cell of the square lattice, i , is occupied by either solvent, in liquid ($l_i = 1, n_i = 0$) or vapor phase ($l_i = 0, n_i = 0$), or by a nanoparticle ($l_i = 0, n_i = 1$). In our implementation, one particle is assumed to occupy 2 \times 2 cell spaces, which is not a crucial parameter, as discussed in the previous studies.^{16,23} Initially, all of the lattice cells without particles are occupied by liquid inside a circular domain and vapor outside it:

$$l_i = \begin{cases} 1 & \text{if } (x_i - R)^2 + (y_i - R)^2 \leq R^2 \\ 0 & \text{if } (x_i - R)^2 + (y_i - R)^2 > R^2 \end{cases} \quad (1)$$

where x_i ($0 \leq x_i \leq 2R$) and y_i ($0 \leq y_i \leq 2R$) are the lattice rows and columns of the i th cell and R is the radius of the circular domain, expressed by an integer number of cells. It is an approximation of the circular domain shape on the discrete square lattice. (See Figure 1.) However, the small shape defects are negligible for a large number of cells because a significant number of perturbations permanently occur at the droplet boundary with the near-equilibrium conditions, hence blurring the boundaries. In the initial step of the simulation, the nanoparticles with a defined concentration are assumed to be uniformly distributed inside the circular wet area of the lattice. The basic configuration mimics the top view of a sessile spherical nanofluid droplet on a substrate. (A tiny droplet with a contact angle of 30° can be seen in the inset of Figure 1.) On

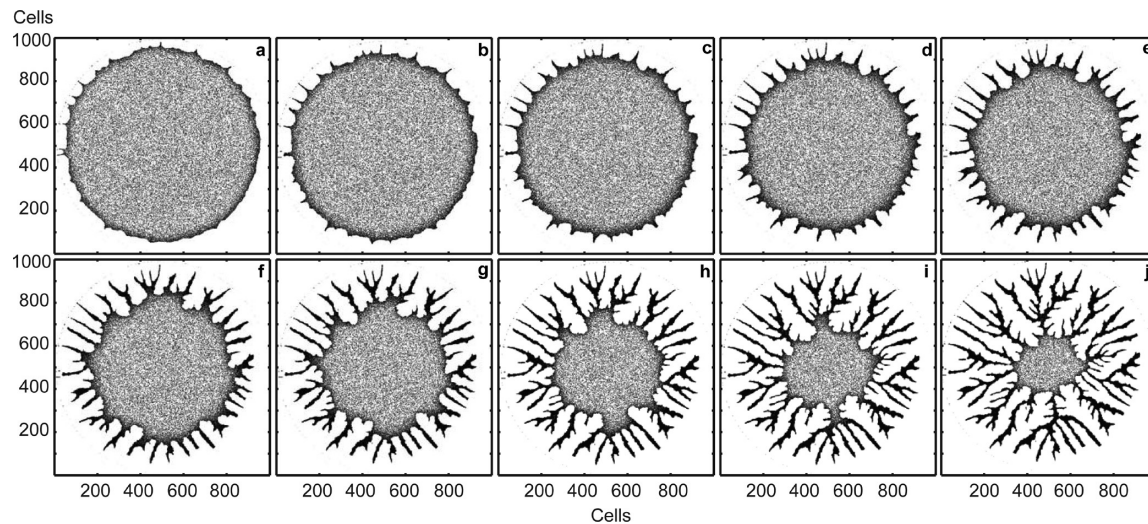


Figure 2. Intermediate steps of the simulation process for the uniform droplet evaporation. The images are captured after (a) 1000, (b) 2000, (c) 3000, (d) 4000, (e) 5000, (f) 6000, (g) 7000, (h) 8000, (i) 9000, and (j) 10 000 MCS, respectively. The particles are shown in black. The simulation parameters are taken as $D = 1000$, $\phi = 20\%$, $N_{\text{move}} = 1$, $kT = 0.2$, $\mu_b = -2.1$, and $J = 1.0 \times 10^{-4}$.

each step of the Monte Carlo process, two possible moves in the system are considered in turn: (1) Perturbation in state of each solvent cell, $l_i \rightarrow 1 - l_i$ and (2) N_{move} random moves of each nanoparticle in the liquid. The value of N_{move} is used to control the rate of nanoparticle diffusion as compared with the solvent evaporation rate. Therefore, one MCS is defined as one attempt to convert the states of all solvent cells, followed by N_{move} attempts to move each nanoparticle. Each mentioned attempt obeys the Metropolis probability:²³

$$p_{\text{acc}} = \min \left[1, \exp \left(-\frac{\Delta E}{kT} \right) \right] \quad (2)$$

where T is the system temperature, k is the Boltzmann constant, p_{acc} is the acceptance probability of the processed move, and ΔE is the system energy change, calculated in eq 2 for the system Hamiltonian

$$E = - \frac{\frac{\varepsilon_{nn}}{2} \sum_{<ij>} n_i n_j + \frac{\varepsilon_{nl}}{2} \sum_{<ij>} n_i l_j + \frac{\varepsilon_{ll}}{2} \sum_{<ij>} l_i l_j}{1 + \sqrt{2}} - \sum_i \mu(i, t) l_i \quad (3)$$

where μ , a function of position i and time t , is the effective chemical potential of the solvent; ε_{nn} , ε_{nb} , and ε_{ll} are the interaction energies for adjacent sites (i,j) filled by (particle, particle), (particle, liquid), or (liquid, liquid), respectively, and j is the index of the lattice cells adjacent to the i th cell; and t is the MCS number. The sums, $\sum_{<ij>}$, are taken for all pairs of the nearest and next-nearest cells. For the next-nearest cells, the interaction coefficients are weighted by a distance factor, $1/\sqrt{2}$. The values of the interaction energies and the chemical potential are nondimensionalized by the ε_{ll} factor. Taking into account the changing thickness profile of the drying droplet, the local effective chemical potential value is assumed to depend on the cell coordinates and time. In the axisymmetric drying process simulation, the chemical potential, μ , depends on the nondimensional distance, r ($0 \leq r \leq 1$), from the center of the circular domain to the processed lattice cell and t

$$\mu(i, t) = f \left(\sqrt{\left(\frac{x_i}{R} - 1 \right)^2 + \left(\frac{y_i}{R} - 1 \right)^2}, t \right) = f(r, t) \quad (4)$$

For the drying process with the receding contact line, it is convenient to initialize the value of the chemical potential function on the three-phase line at zero time moment, $f(1,0) = \mu_b$, and hence μ_b is the initial boundary value. Moreover, the equilibrium chemical potential is known to be -2.0 for the 2D lattice-gas without particles²³ and is less than -2.0 in the presence of the suspended particles.¹⁶ Therefore, we use the condition, $\mu_b < -2.0$, in the simulations. In the bulk of the droplet, the chemical potential is assumed to be higher initially than μ_b because this area remains fully covered by a thicker liquid layer until the drying front reaches it. Note that the effective chemical potential term was discussed to be influenced by the thickness-dependent disjoining pressure¹⁰ and curvature-dependent Laplace pressure.¹⁷ Because the Laplace pressure term depends on the liquid layer curvature while the disjoining pressure term depends on the layer thickness itself,¹⁷ the disjoining pressure term can be assumed to be negligible because the droplet thickness is much greater than the intermolecular distance, as indicated by Frastia et al.¹⁷ Then, the Laplace pressure term is related to the second differential of the thickness of the spherical droplet cap with respect to the lattice radius; hence it can be expected that the chemical potential approaches a linear function as the contact angle is $\leq 30^\circ$. (See the inset in Figure 1.) For simplicity, we assume that the chemical potential can be approximated with a linear function in this study, taking the highest value at the domain center and the lowest at the boundary:

$$\mu_1(r) = (\mu_0 - \mu_b)(1 - r) + \mu_b \quad (5)$$

where $\mu_1(r) = f(r,0)$, which is the profile of chemical potential at the first step of simulation. The initial boundary chemical potential, $\mu_1(1) = \mu_b$, and the initial value at the domain center, $\mu_1(0) = \mu_0$. We assume $\mu_0 > \mu_b$. In the simulation, the contact line of r shrinks with evaporation. In the study of the slow evaporation to mimic the natural drying process of the droplets, $\mu(r,t)$ is assumed to decrease over the whole wetting domain with the constant rate, $J > 0$, to the time variable, t : $\mu(r,t) =$

$\mu_1(r) = Jt$. Finally, eq 6 can be obtained for the effective chemical potential and used throughout the simulation run; the parameter J can be controlled to change the evaporation rate in the simulation.

$$\mu(r, t) = (\mu_0 - \mu_b)(1 - r) + \mu_b - Jt \quad (6)$$

RESULTS AND DISCUSSION

Symmetrical Drying Process. The first simulation has been conducted with the parameter settings: $D = 1000$, $\phi = 20\%$, $N_{move} = 1$, $kT = 0.2$, $\mu_b = -2.1$, and $J = 1.0 \times 10^{-4}$. The intensively branched patterns are obtained, as seen in Figure 2. The sequence of images illustrates the progression of a spherical nanofluid droplet drying simulation. The simulation process starts with the uniform particle distribution inside the circular domain (Figure 2a); consequently, the shrinking drying front deposits particles into finger-like structures toward the droplet center (Figure 2d–j).

Figure 3a illustrates a sample result from the experimental observation of drying a nanofluid sessile droplet. It demon-

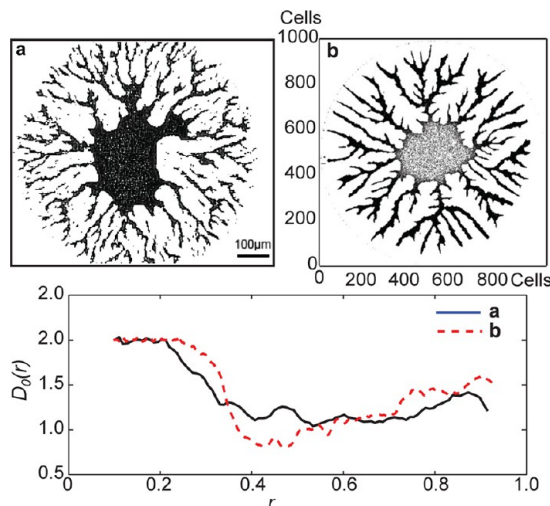


Figure 3. (a) Experimentally recorded image of a dried nanoparticle aggregate. The pattern was formed after evaporation of a nanofluid sessile droplet. The nanofluid was prepared from the 25 nm copper nanoparticles dispersed well in the deionized water. (b) Snapshot of the Monte Carlo simulation taken after 10 000 MCS. The parameter values have been taken: $D = 1000$, $\phi = 0.2$, $N_{move} = 1$, $kT = 0.2$, $J = 1.0 \times 10^{-4}$, and $\epsilon_{nn} = \epsilon_{nl} = 1.5$. (c) Mass–radius growth exponent comparison for the structures from panels a and b.

strates the formation of macroscopic branched structures. The fingers extended evenly from the center toward the edge of the drop. The shown drying pattern was obtained from natural evaporation of ~ 1 mm sessile droplet on a clean silicon wafer; the droplet was taken from the copper (25 nm) water-based nanofluids at the mass concentration of 0.1%. The structure shows a crucial difference from the conventional coffee-ring pattern.^{6,28} The formation of branches starts from the fingering contact line instabilities,¹⁶ resembling the appearance of those observed in the spreading surfactant solutions.²⁹ It is suggested that the capillary flow, responsible for the coffee-ring formation,⁶ was not significant enough to cause the initial contact line pinning for a given droplet size under these experimental conditions. As a result, the three-phase contact line was continuously shrinking and pulling the particles in the

direction toward the center, eventually leading to the formation of a global branched particle aggregate.

The comparison between the isotropic experimental and the simulated images shows a good agreement in trend. (See Figure 3a,b.) The particles tend to aggregate into a well-distributed intensively branched structure with dense packing near the center. We have stopped the simulation after 10 000 MCS and captured the particle positions at the particular time moment because it resembles the experimental observation that droplet shrinking halts.

For the detailed comparison, we calculate the mass–radius growth exponent of both the experimental and simulated structures. This metric D_0 of an arbitrary pattern can be estimated from the mass–radius relation²⁷

$$N(r) \approx r^{D_0} \quad (7)$$

where $N(r)$ is the number of particles contained inside the circle of radius r . Because the structures investigated are not scale-invariant, the value of $D_0(r)$ depends on the distance from the domain center. In the case of self-similar fractals, the metric $D_0(r)$ would be scale-invariant and characterize the fractal dimension of the observed structures. Now the problem is equivalent to the calculation of numerical derivative:

$$D_0(r) = d[\log(N(r))]/dr \quad (8)$$

The comparison results are summarized in Figure 3 for the symmetrical structures. The average and local metric values, $D_0(r)$, recall each other in the experiment and simulation (Figure 3c), pointing to a rather similar distribution of particles inside the structure. The detailed effects of the parameters are discussed in the parameter study.

Parameter Study of KMC Model. A further analysis of the parameter effects has been performed. To make the results comparable, we have fixed a certain time point, 10 000 MCS, and captured all of the simulation results simultaneously. Because we investigate the model behavior inside the circular domain, it is important to show the dependence of drying pattern on the domain diameter, $D (= 2R)$. Figure 4 shows that the patterns range from disk-like closely packed structures for the small lattices (see Figure 4a,f) to highly branched aggregates for the large lattices (see Figure 4e,j).

The second parameter study indicates the dependence on the rate of chemical potential change, J , and the initial boundary chemical potential value, μ_b . We compare the results after 10 000 MCS, and Figure 5 demonstrates the particle self-assembly at the time moment. Figure 5a–e shows that a low J value corresponds to the position of drying front far from the domain center, whereas a high J value results in a fast contact line motion, as the drying front reaches the domain center by 10 000 MCS for each μ_b value. (See Figure 5k–o.) Also note that a higher value of μ_b leads to a smooth shape of the branches, shown in Figure 5e,j,o, whereas in the opposite cases the multiple side branches arise, as indicated in Figure 5k–l. It can be explained with the observation that the combination of high μ_b and low J values results in slowing down the dewetting front motion because the initial large difference of the chemical potential between the center and boundary of the droplet is not compensated by a low J rate of decay. The opposite combination correspondingly leads to the accelerating contact line shrinking, subsequently associated with the side branch forming. It was indicated by Vancea et al.¹⁶ that the number of fingers for moving drying front depended on the chemical potential and hence on the motion velocity. Applying the rule

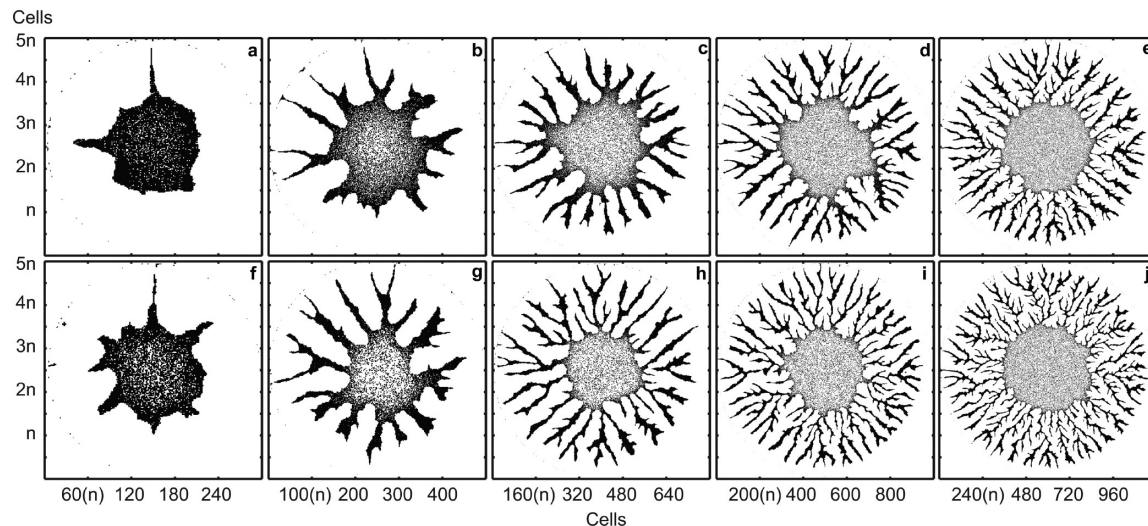


Figure 4. KMC simulation results in an open circular domain for different values of the domain size, D , and the particle interaction energy, ϵ_{mm} . Parameter values: (a–e) $\epsilon_{mm} = 1.5$ and (f–j) $\epsilon_{mm} = 1.55$; (a,f) $D = 300$, (b,g) $D = 500$, (c,h) $D = 750$, (d,i) $D = 1000$, and (e,j) $D = 1250$. The other parameters: $J = 1.0 \times 10^{-4}$, $\mu_b = -2.1$, and MCS = 10 000. n in the Figure depends on the size with a value of 60, 100, 160, 200, and 240.

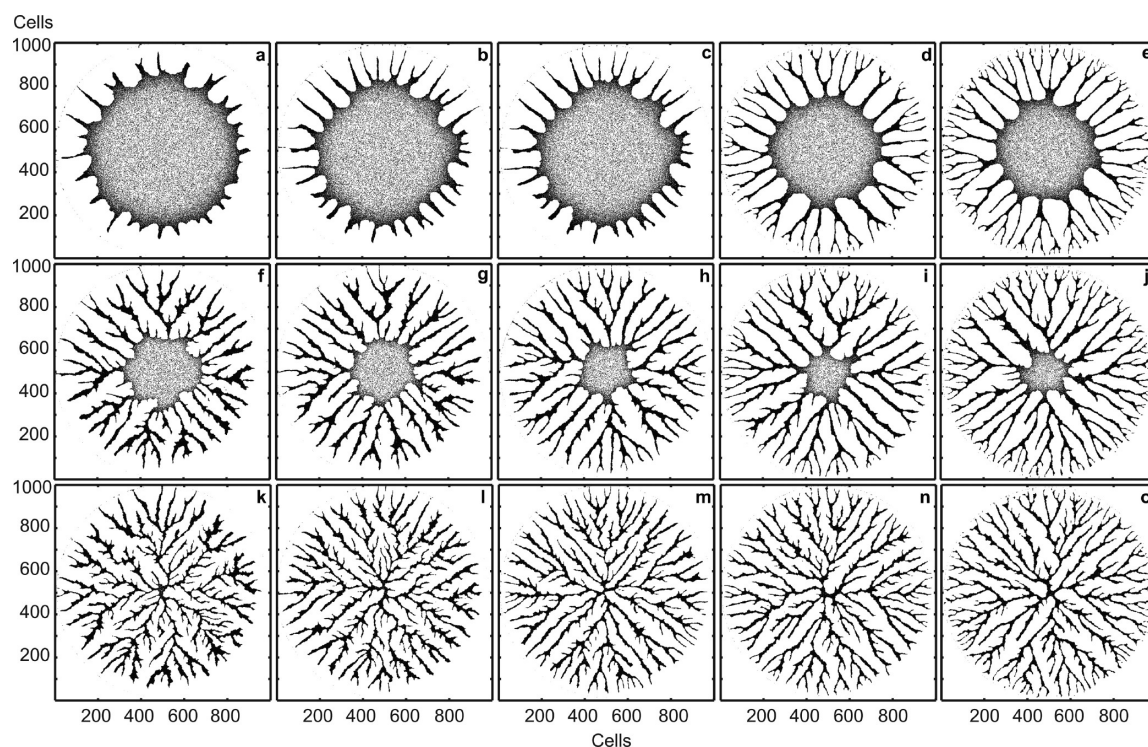


Figure 5. KMC simulation results in an open circular 1000×1000 domain for the different initial boundary values of chemical potential, μ_b , and the rates of chemical potential change, J . Parameter values: (a–e) $J = 0.5 \times 10^{-4}$, (f–j) $J = 1.0 \times 10^{-4}$, and (k–o) $J = 1.5 \times 10^{-4}$; (a,f,k) $\mu_b = -2.1$, (b,g,l) $\mu_b = -2.2$, (c,h,m) $\mu_b = -2.3$, (d, i, n) $\mu_b = -2.4$, and (e, j, o) $\mu_b = -2.5$. The other parameters: $\epsilon_{mm} = 1.5$ and MCS = 10 000. The particles are shown in black.

to our cases of the accelerating drying front, we can explain the emergence of new side branches in the resulting structure in Figure 5.

The last series of simulations aims to investigate the influence of the particle interaction energy, ϵ_{mm} , and the particle mobility rate, N_{move} . Figure 6 suggests that increasing N_{move} acts similarly as decreasing the particle interaction energy, ϵ_{mm} . Comparing, for example, the images in Figure 6a,c,h proves that both decreasing ϵ_{mm} and increasing N_{move} leads to fewer in number but thicker branches. This behavior could be explained by the

assumption that the mobile particles are collected more easily by the drying front and pulled toward the domain center. Decreasing the interaction energy causes the similar effect: the better distributed particles tend to move along the drying front rather than to aggregate into the branches and remain behind. These trends were also discussed by Vancea et al.¹⁶ for a straight drying front. The additional results of the parameter study can also be found in the Supporting Information S1.

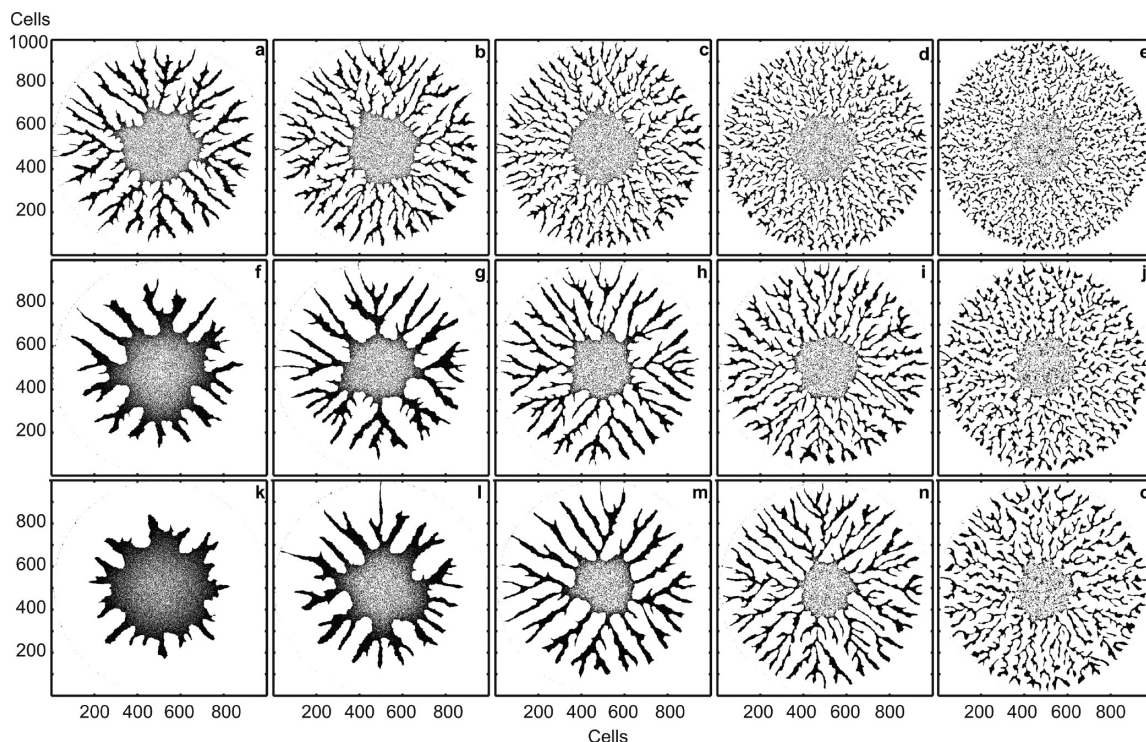


Figure 6. KMC simulation results in an open circular 1000×1000 domain for the different particle mobility rate, N_{move} , and the particle interaction energy, ϵ_{nn} . Parameter values: $N_{\text{move}} = 1$ (a–e), $N_{\text{move}} = 3$ (f–j), and $N_{\text{move}} = 5$ (k–o); $\epsilon_{nn} = 1.5$ (a,f,k), $\epsilon_{nn} = 1.55$ (b,g,l), $\epsilon_{nn} = 1.6$ (c,h,m), $\epsilon_{nn} = 1.65$ (d,i,n), and $\epsilon_{nn} = 1.7$ (e,j,o); $\phi = 10\%$, $J = 1.0 \times 10^{-4}$, $kT = 0.2$. Images are captured after 10 000 MCS; the particles are shown in black.

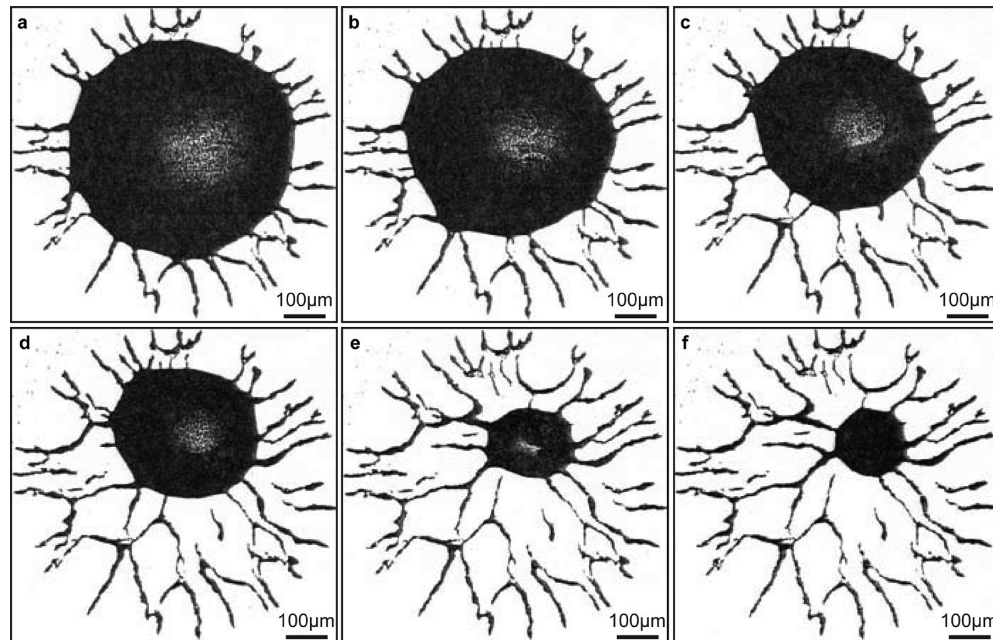


Figure 7. Case study 1: an asymmetrically drying sessile droplet of 0.1% copper–water suspension. Images are captured by the optical microscope; the substrate used is a silicon wafer.

Asymmetrical Drying. Asymmetrical droplet drying, often observed in the experiments, might result from the uneven evaporation rate^{30–32} or contact line dynamics.

The example patterns presented in Figures 7 and 8 show the asymmetrical formation of the branched structures from evaporating the sessile droplets with a diameter of about 1 mm or less. In the experiments we continuously recorded the drying of 0.1% copper–water nanofluid droplets on a clean

silicon wafer. The shrinking process is displayed, and a detailed view of the branch development can be observed. The results show that the structure morphology maintains its branched asymmetrical structure in both of the cases, but the formation of thinner branches with multiple ruptures is observed in Figure 8. We can see from both Figure 7 and Figure 8 that the drying process starts unevenly at the different sides of the droplet. Branches are formed in both the cases from the beginning of

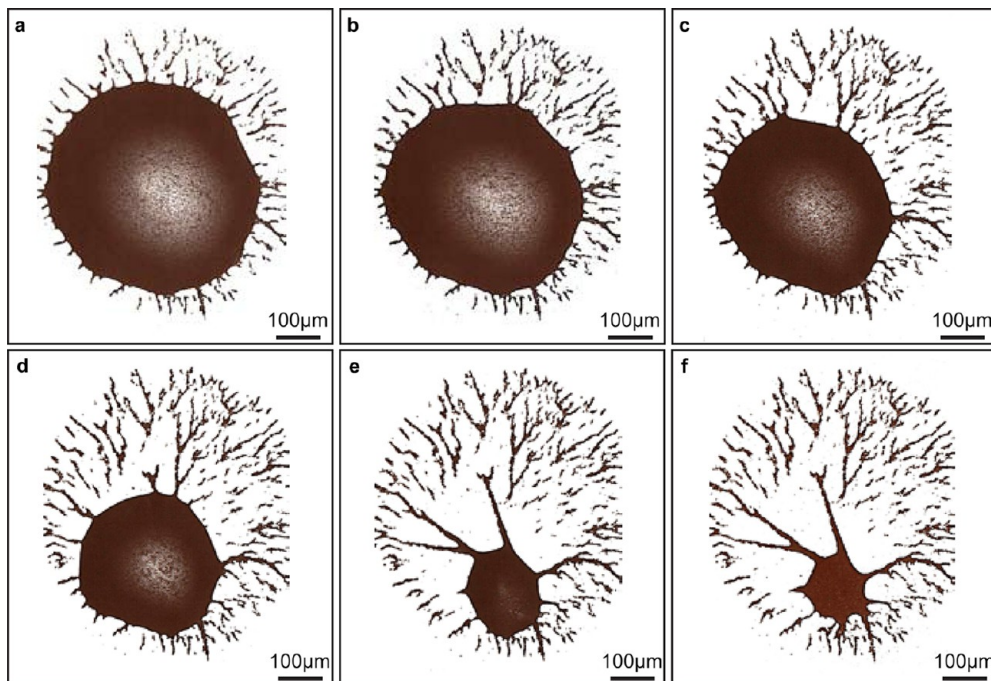


Figure 8. Case study 2: an asymmetrically drying sessile droplet of 0.1% copper–water suspension. Images are captured by the optical microscope; the substrate used is a silicon wafer.

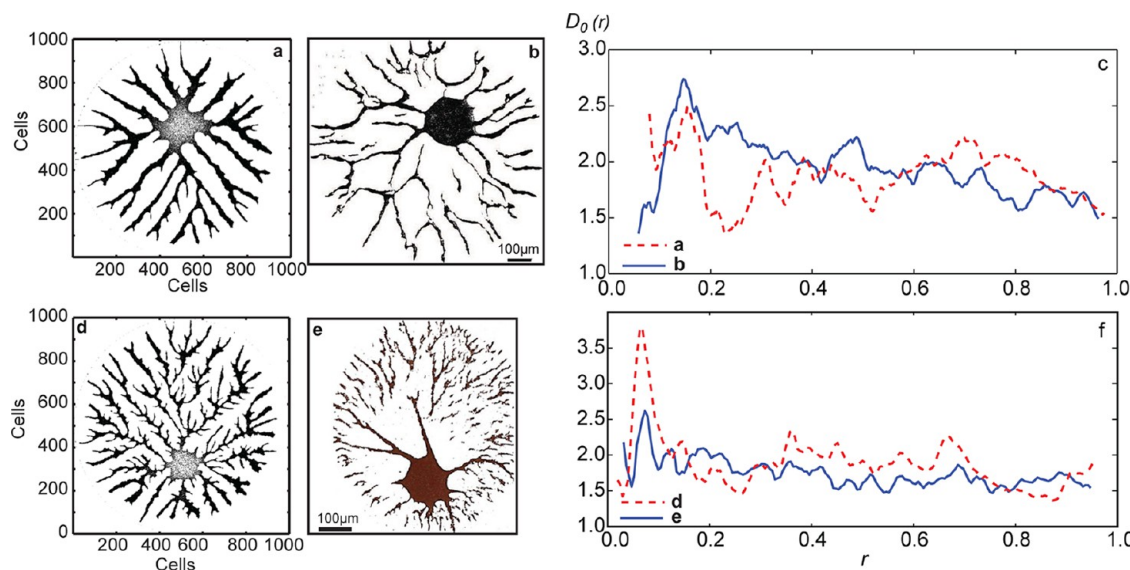


Figure 9. Comparison of the experimental and simulated structures, resulting from nonuniform drying process. (a) Simulated structure, captured after 22 000 MCS. The parameter values: $D = 1000$, $\phi = 20\%$, $N_{\text{move}} = 1$, $kT = 0.2$, $J = 0.5 \times 10^{-4}$, $x_0 = 500$, and $y_0 = 333$. (b) Experimental result of the asymmetrically self-assembled dried copper particles from Figure 7f. (c) Mass–radius growth exponent comparison for the structures from panels a and b. (d) Simulated structure, captured after 13 500 MCS. The parameter values: $D = 1000$, $\phi = 20\%$, $N_{\text{move}} = 1$, $kT = 0.2$, $J = 1.0 \times 10^{-4}$, $x_0 = 500$, $y_0 = 333$. (e) Experimental result of the asymmetrically self-assembled dried copper particles in Figure 8f. (f) Mass–radius growth exponent comparison for the structures from panels d and e.

the droplet shrinking (see Figures 7a and 8a), but a higher number of thinner and shorter branches are demonstrated in Figure 8c, as compared with the thicker structure formed in Figure 7d. Eventually, the drying process stops at the point far from the initial droplet center in both of the experiments, as shown in Figures 7f and 8f. The question for the further discussion here is that different patterns arise from the nanofluids under the same concentration with a slight difference on initial droplet size. By evaluating the possible factors affecting the drying patterns, we assume that the highest

effect may come from the environmental conditions related to the simulation parameter, J . The detailed simulation studies can be found in the Supporting Information S1.

As we compare the results, an agreement in trend is found between the simulation in Figure 9a and the experimental result in Figure 9b, as indicated in Figure 9c for Case 1. The length of branches is significantly greater on one side for both of the structures. Another comparison is shown in Figure 9d–f. It features the experimental result of drying the 0.1% copper nanofluid droplet (Figure 9e); the full drying process is shown

in Figure 8, and the result of the asymmetric simulation with a high chemical potential rate of change $J = 10^{-4}$. (See Figure 9d.) The full simulation process is displayed in the Supporting Information S1, Figure S4.) Both of the comparisons demonstrate the similarity on drying dynamics and final morphology of nanoparticle patterns.

We have calculated the mass–radius growth exponent metric for the asymmetrical simulated and the experimental results as well. The higher average D_0 of the simulated structures in Figure 9f might result from the thicker side branches, thus contributing to the faster mass–radius growth. The local behavior of the curves with a similar trend for the experiments and simulations in Figure 9c,f reflects the similar branching topology of the structures in Figure 9a,b and Figure 9d,e respectively. Further experimental work in this direction will probably clarify the stability of the observed patterns.

CONCLUSIONS

The branched nanoparticle aggregates were found after the drying of a sessile droplet of the copper–water nanofluids. The KMC approach has been developed to simulate the formation of drying patterns. From the qualitative structure similarity and the calculated statistical metrics, D_0 , the branched structures from the simulations and experiments can recall each other. The effects of the circular domain diameter (D), the particle coverage (ϕ), the rate of chemical potential change (J), the particle interaction energy (ϵ_{nn}), the diffusive mobility (N_{move}), and the initial boundary value (μ_b) on the particle patterning have been investigated in detail. All of the involved parameter values are nondimensional and provide a relative comparable estimation of the experimental conditions. The model is intuitively simple and can provide useful behavioral trends to control the experiments. The future work has been started in more sophisticated systems, including the effects such as capillary flow⁶ and Marangoni convection.^{30,33}

ASSOCIATED CONTENT

Supporting Information

The additional parameter study results are in Supporting Information S1. Supporting Information S2 describes the simulation process of the droplet drying: Supplementary Movie 1, Supplementary Movie 2, and Supplementary Movie 3. This material is available free of charge via the Internet at <http://pubs.acs.org>.

AUTHOR INFORMATION

Corresponding Author

*E-mail: feiduan@ntu.edu.sg. Phone: +65 67905510. Fax: +65 67924062.

Notes

The authors declare no competing financial interest.

ACKNOWLEDGMENTS

We acknowledge the support of A*Star Public Sector Funding (1121202010). We also acknowledge the essential help from the NTU student, Ms. Hui Ying Ow, in conducting the experimental work.

REFERENCES

- (1) Yosef, G.; Rabani, E. Self-Assembly of Nanoparticles into Rings: A Lattice-Gas Model. *J. Phys. Chem. B* **2006**, *110*, 20965–20972.
- (2) Murray, C. B.; Kagan, C. R.; Bawendi, M. G. Self-Organization of CdSe Nanocrystallites into 3-Dimensional Quantum-Dot Superlattices. *Science* **1995**, *270*, 1335–1338.
- (3) Freeman, R. G.; Grabar, K. C.; Allison, K. J.; Bright, R. M.; Davis, J. A.; Guthrie, A. P.; Hommer, M. B.; Jackson, M. A.; Smith, P. C.; Walter, D. G.; Natan, M. J. Self-Assembled Metal Colloid Monolayers: An Approach to SERS Substrates. *Science* **1995**, *267*, 1629–1632.
- (4) Andres, R. P.; Bielefeld, J. D.; Henderson, J. I.; Janes, D. B.; Kolagunta, V. R.; Kubiak, C. P.; Mahoney, W. J.; Osifchin, R. G. Self-Assembly of a Two-Dimensional Superlattice of Molecularly Linked Metal Clusters. *Science* **1996**, *273*, 1690–1693.
- (5) Kuncicky, D. M.; Bose, K.; Costa, K. D.; Velev, O. D. Sessile Droplet Templating of Miniature Porous Hemispheres from Colloid Crystals. *Chem. Mater.* **2007**, *19*, 141–143.
- (6) Deegan, R. D.; Bakajin, O.; Dupont, T. F.; Huber, G.; Nagel, S. R.; Witten, T. A. Capillary Flow as the Cause of Ring Stains from Dried Liquids. *Nature* **1997**, *389*, 827–829.
- (7) Bigioni, T. P.; Lin, X.-M.; Nguyen, T. T.; Corwin, E. I.; Witten, T. A.; Jaeger, H. M. Kinetically Driven Self Assembly of Highly Ordered Nanoparticle Monolayers. *Nat. Mater.* **2006**, *5*, 265–270.
- (8) Deegan, R. D.; Bakajin, O.; Dupont, T. F.; Huber, G.; Nagel, S. R.; Witten, T. A. Contact Line Deposits in an Evaporating Drop. *Phys. Rev. E* **2000**, *62*, 756–765.
- (9) Deegan, R. D. Pattern Formation in Drying Drops. *Phys. Rev. E* **2000**, *61*, 475–485.
- (10) Stannard, A.; Martin, C. P.; Pauliac-Vaujour, E.; Moriarty, P.; Thiele, U. Dual-Scale Pattern Formation in Nanoparticle Assemblies. *J. Chem. Phys. C* **2008**, *112*, 15195–15203.
- (11) Pauliac-Vaujour, E.; Moriarty, P. Meniscus-Mediated Organization of Colloidal Nanoparticles. *J. Phys. Chem. C* **2007**, *111*, 16255–16260.
- (12) Martin, C. P.; Blunt, M. O.; Pauliac-Vaujour, E.; Stannard, A.; Moriarty, P.; Vancea, I.; Thiele, U. Controlling Pattern Formation in Nanoparticle Assemblies via Directed Solvent Dewetting. *Phys. Rev. Lett.* **2007**, *99*, 116103.
- (13) Crivoi, A.; Duan, F. Evaporation-Induced Formation of Fractal-Like Structures from Nanofluids. *Phys. Chem. Chem. Phys.* **2012**, *14*, 1449–1454.
- (14) Brutin, D.; Sobac, B.; Loquet, B.; Sampol, J. Pattern Formation in Drying Drops of Blood. *J. Fluid Mech.* **2011**, *667*, 85–95.
- (15) Yakhno, T. Salt-Induced Protein Phase Transitions in Drying Drops. *J. Colloid Interface Sci.* **2008**, *318*, 225–230.
- (16) Vancea, I.; Thiele, U.; Pauliac-Vaujour, E.; Stannard, A.; Martin, C. P.; Blunt, M. O.; Moriarty, P. J. Front Instabilities in Evaporatively Dewetting Nanofluids. *Phys. Rev. E* **2008**, *78*, 041601.
- (17) Frastia, L.; Archer, A. J.; Thiele, U. Dynamical Model for the Formation of Patterned Deposits at Receding Contact Lines. *Phys. Rev. Lett.* **2011**, *106*, 077801.
- (18) Martin, C. P.; Blunt, M. O.; Moriarty, P. Nanoparticle Networks on Silicon: Self-Organized or Disorganized? *Nano Lett.* **2004**, *4*, 2389–2392.
- (19) Pauliac-Vaujour, E.; Stannard, A.; Martin, C. P.; Blunt, M. O.; Notingher, I.; Moriarty, P.; Vancea, I.; Thiele, U. Fingering Instabilities in Dewetting Nanofluids. *Phys. Rev. Lett.* **2008**, *100*, 176102.
- (20) Robbins, M. J.; Archer, A. J.; Thiele, U. Modelling the Evaporation of Thin Films of Colloidal Suspensions Using Dynamical Density Functional Theory. *J. Phys.: Condens. Matter.* **2011**, *23*, 415102.
- (21) Warner, M. R. E.; Craster, R. V.; Matar, O. K. Surface Patterning via Evaporation of Ultrathin Films Containing Nanoparticles. *J. Colloid Interface Sci.* **2003**, *267*, 92–110.
- (22) Lyushnin, A. V.; Golovin, A. A.; Pismen, L. M. Fingering Instability of Thin Evaporating Liquid Films. *Phys. Rev. E* **2002**, *65*, 021602.
- (23) Rabani, E.; Reichman, D. R.; Geissler, P. L.; Brus, L. E. Drying-Mediated Self-Assembly of Nanoparticles. *Nature* **2003**, *426*, 271–274.
- (24) Sztrum, C. G.; Hod, O.; Rabani, E. Self-Assembly of Nanoparticles in Three-Dimensions: Formation of Stalagmites. *J. Phys. Chem. B* **2005**, *109*, 6741–6747.

- (25) Kwek, D.; Crivoi, A.; Duan, F. Effects of Temperature and Particle Size on the Thermal Property Measurements of Al_2O_3 -Water Nanofluids. *J. Chem. Eng. Data* **2010**, *55*, 5690–5696.
- (26) Duan, F.; Kwek, D.; Crivoi, A. Viscosity Affected by Nanoparticle Aggregation in Al_2O_3 -Water Nanofluids. *Nanoscale Res. Lett.* **2011**, *6*, 248.
- (27) Caserta, F.; Eldred, W. D.; Fernandez, E.; Hausman, R. E.; Stanford, L. R.; Bulderev, S. V.; Schwarzer, S.; Stanley, H. E. Determination of Fractal Dimension of Physiologically Characterized Neurons in Two and Three Dimensions. *J. Neurosci. Methods* **1995**, *56*, 133–144.
- (28) Yunker, P. J.; Still, T.; Lohr, M. A.; Yodh, A. G. Suppression of the Coffee-Ring Effect by Shape-Dependent Capillary Interactions. *Nature* **2011**, *476*, 308–311.
- (29) Cachile, M.; Cazabat, A. M. Spontaneous Spreading of Surfactant Solutions on Hydrophilic Surfaces. *Langmuir* **1999**, *15*, 1515–1521.
- (30) Duan, F.; Ward, C. A. Investigation of Local Evaporation Flux and Vapor-Phase Pressure at an Evaporative Droplet Interface. *Langmuir* **2009**, *25*, 7424–7431.
- (31) Duan, F. Local Evaporation Rate Effected by Thermocapillary Convection at Evaporating Droplet. *J. Phys. D: Appl. Phys.* **2009**, *42*, 102004.
- (32) Thompson, I.; Duan, F.; Ward, C. A. Absence of Marangoni Convection at Marangoni Numbers Above 27,000 During Water Evaporation. *Phys. Rev. E* **2009**, *80*, 056308.
- (33) Ward, C. A.; Duan, F. Turbulent Transition of Thermocapillary Flow Induced by Water Evaporation. *Phys. Rev. E* **2004**, *69*, 056308.